Electronic Supplementary Material (ESI) for Inorganic Chemistry Frontiers.

Supporting Information

Design of Charge Transfer Channels: Defective TiO_2/MoP Supported on Carbon Cloth for Solar-Light-Driven Hydrogen Generation

Qianqian Tian,[a] Shasha Yi,[b] Chuanqi Li,[a] Yan Liu,[a] Zhulin Niu,[a] Xinzheng Yue*[a] and Zhongyi Liu*[a]

[a]College of Chemistry, Zhengzhou University, Zhengzhou 450001, China.

[b]School of Materials Science and Engineering, Zhengzhou University, Zhengzhou 450001, China.

*Corresponding authors

E-mail addresses: yuexz@zzu.edu.cn (Xinzheng Yue), lzy2020lsch@outlook.com (Zhongyi Liu)

Table of contents

1. Experimental section

1.1 Materials

Ammonium molybdate ($(NH_4)_6Mo_7O_{24}\cdot 4H_2O$, ≥99%), ammonium phosphate ($(NH_4)_2HPO_4$, ≥99%), acetone (C_3H_6O, ≥99.5%), barium sulfate ($BaSO_4$, 99%) and nitric acid (HNO_3, ≥68%) were purchased from Tianjin Kermel Chemical Reagent Co., Ltd. Acetic acid (CH_3COOH, ≥90%), citric acid ($C_6H_8O_7$, ≥99.5%) and iodine (I_2, ≥99.8%) were bought from Tianjin Fengchuan Chemical Reagent Co., Ltd. Potassium hydroxide (KOH, ≥85%), ethanol (CH_3CH_2OH, ≥95.0%), tetrabutyl titanate (TBOT, ≥98.0%) and triethanolamine (78%) were purchased from Shanghai Chemical Reagent Co., Ltd. The deionized water with a resistivity of 18.2 MΩ·cm was obtained by reverse osmosis followed by ion-exchange and filtration. Carbon cloth (CC, WOS1009) was commercially available from Nantong Co., Ltd. Before experiment, the CC (1 cm × 1.5 cm) was treated with 0.5 M HNO_3, after which it was ultrasonically rinsed in water and ethanol for several times until its pH value adjusted to 7 and then dried by Ar stream. All chemicals used in this study are of analytical grade without further purification. The N_2/H_2 gas mixture (10 vol% of H_2), N_2 and Ar (99.999%) were provided by Henan Yuanzheng Technology Development Co., Ltd.

1.2 Characterization

The crystal phase compositions of the as-prepared samples were examined with X-ray di□raction (XRD) with a Bruker XRD-D8 Advance di□ractometer at 40 kV and 40 mA, in which Cu Kα was used as radiation (λ = 1.54056 Å). X-ray photoelectron spectroscopy (XPS) was conducted on a Thermo VG Scientific ESCALAB 250 with Al Kα X-ray source. All binding energies were calibrated to adventitious carbon peak value of 284.8 eV. The field-emission scanning electron microscope (FESEM) and energy-dispersive X-ray (EDX) elemental mapping were obtained by JEOL JSM 6700F

electron microscope. Transmission electron microscopy (TEM) and selected area electron di□raction (SAED) were operated on a Tecnai G2 F20 TEM microscope (FEI Company). The Brunauer-Emmett-Teller (BET) measurements were analyzed on JW BK112 specific surface area pore size analyzer (JWGB SCI&TECH). The ultraviolet-visible di□use reflectance spectra (UV-vis DRS) were recorded using Shimadzu UV-3600 spectrophotometer equipped with an integrating sphere in the wavelength range of 300-800 nm. Raman spectra were carried out by a laser Raman spectrometer (LabRAM HR Evo) at an excitation wavelength of 532 nm in Raman shift range of 100-2000 cm^{-1}. The electron paramagnetic resonance (EPR) spectra were collected via a BRUCER EMXplus-9.5/12 spectrometer at 9.44 GHz at 298 K. The photoluminescence (PL) emission spectra were performed on a fluorescence spectrophotometermeter (HITACHI F-4600) with an excitation wavelength of 325 nm. Time-resolved photoluminescence (TRPL) spectra were obtained via a transient fluorescence spectrometer (FLS980), whose excitation wavelength is 530 nm. Surface photovoltage (SPV) measurements contain a 500 W Xe lamp (CHF-XM-500 W, Global Xenon Lamp Power) equipped with a grating monochromator as light source, a computer, a lock-in amplifier (SR830-D SP) with a light chopper (SR540) and a photovoltaic cell with fluorine-doped tin oxide (FTO) electrode-mica-sample-FTO structure. Before SPV test, the system was calibrated by a DSI200 UV enhanced silicon detector to eliminate the possible phase shift not correlated to the SPV response. The phase retardation can reflect the kinetics of SPV response. Transient photovoltage (TPV) signals were recorded on digital phosphor oscilloscope (TDS 5054, Tektronix) with an excitation wavelength of 355 nm. The intensity of the pulse was controlled with a neutral grey filter and determined with a Joule meter (Starlite, Ophir, Inc.).

1.3 (Photo)electrochemical measurements

Typically, the electrochemical and photoelectrochemical (PEC) measurements were carried out on an electrochemical analyzer (RST electrochemical workstation) using a three-electrode system, where the as-prepared CC-based photocatalyst, Pt wire and Ag/AgCl (saturated KCl) were served as the working electrode, counter electrode and reference electrode, respectively. For electrochemical and PEC measurements, 1 M KOH aqueous solution (pH 13.6) was used as the electrolyte. Linear sweep voltammetric (LSV) curves were recorded in the potential range of −0.8 to −1.6 V *vs*. Ag/AgCl in dark condition with the scan rate of 50 mV s^{-1}. For PEC test, a 300 W Xe lamp (CEL-HXF300, Beijing China Education Au-light Co., Ltd) equipped with an AM 1.5G optical filter to simulate solar light. Electrochemical impedance spectroscopy (EIS) was conducted under light irradiation with an amplitude of 5 mV over the frequency range from 100 kHz to 0.1 Hz at potential of 0 V *vs*. Ag/AgCl. Mott-Schottky (M-S) plots were recorded over an AC frequency of 1000 Hz in dark condition to obtain the types of semiconductors and flat band potentials. Current-time (*i-t*) curves were conducted at 0 V *vs*. Ag/AgCl by switching on/off light for every 30 s.

2. Supplementary Figures

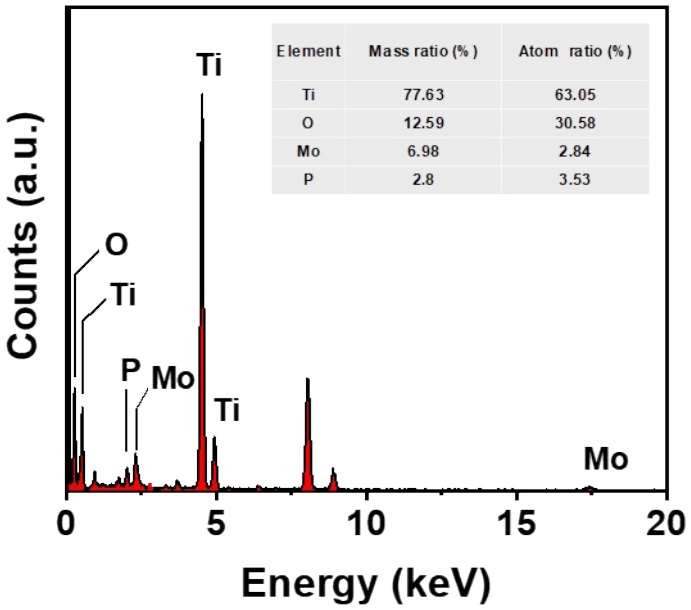

Fig. S1 EDX spectrum of TiO_2/MoP/CC specimen. Inset summarizes the element contents of Ti, O, Mo and P.

In Fig. S1, it is evident that Mo, P, Ti and O elements exist in TiO_2/MoP/CC.

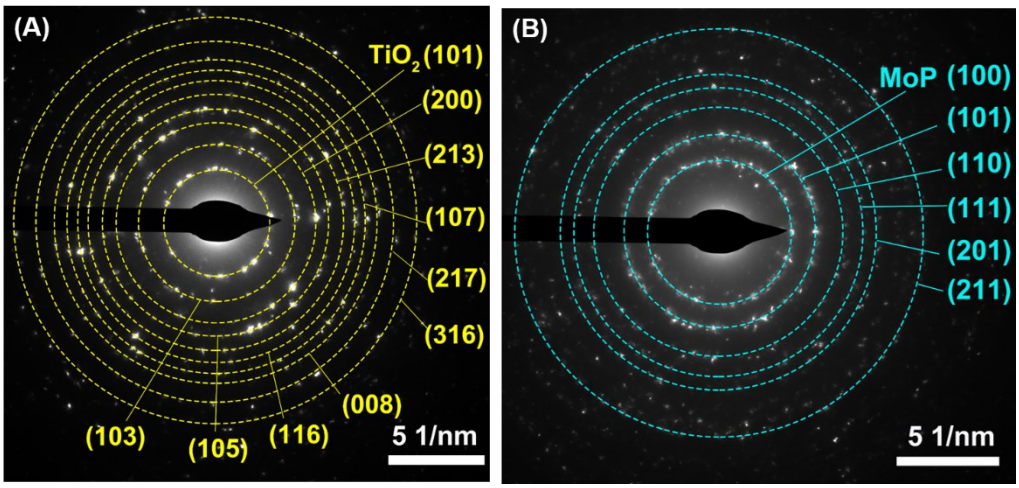

Fig. S2 SAED patterns of (A) TiO_2/CC and (B) MoP/CC samples.

In Fig. S2, diffraction rings of TiO_2 and MoP can be clearly observed in TiO_2/CC and MoP/CC samples, respectively. These results reveal the good crystallinity characteristic of both TiO_2 and MoP.

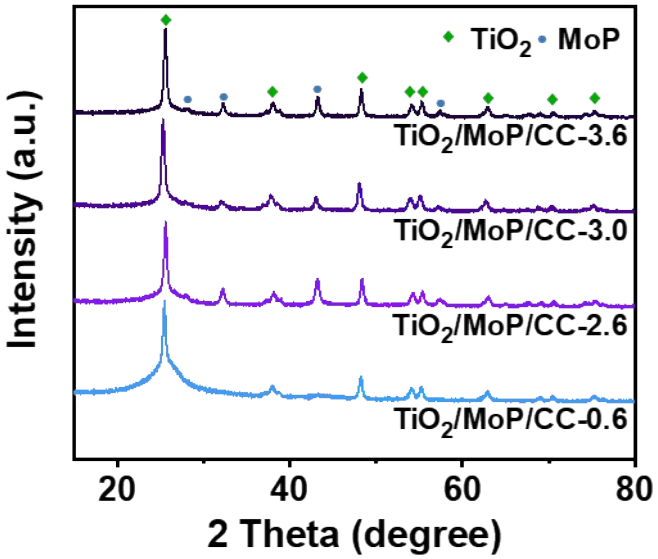

Fig. S3 XRD patterns of TiO_2/MoP/CC-*x* (*x* = 0.6, 2.6, 3.0 and 3.6) samples.

Fig. S3 shows the XRD patterns of TiO_2/MoP/CC-*x* (*x* = 0.6, 2.6, 3.0 and 3.6) samples. No XRD peaks of MoP can be detected in TiO_2/MoP/CC-0.6, attributing to its low content. As the value of *x* increases, the signal intensity of MoP in hybrid catalysts enhance gradually.

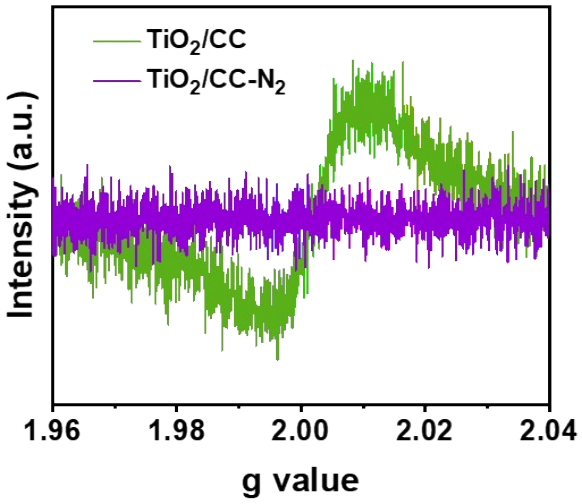

Fig. S4 Electron paramagnetic resonance (EPR) spectra of TiO_2/CC and TiO_2/CC-N_2.

Fig. S4 shows the EPR spectra of TiO_2/CC and TiO_2/CC-N_2 samples. It can be clearly seen that no EPR signal is detected in TiO_2/CC-N_2.

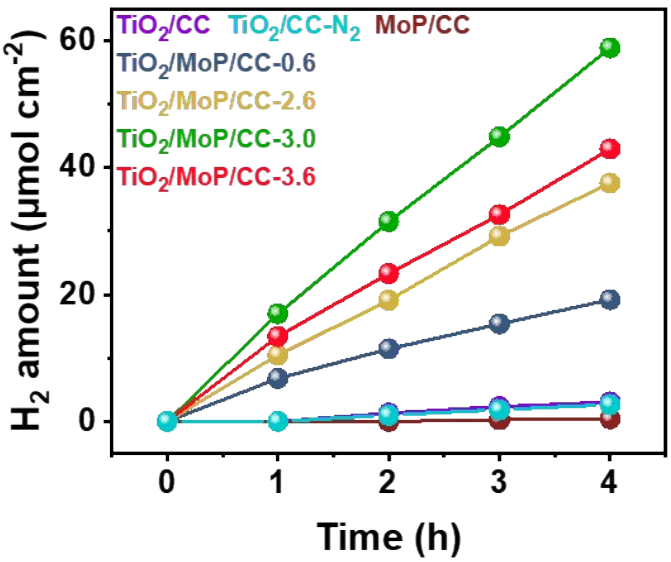

Fig. S5 Photocatalytic H_2 evolution performances of TiO_2/CC, TiO_2/CC-N_2, MoP/CC and TiO_2/MoP/CC-*x* (*x* = 0.6, 2.6, 3.0 and 3.6) samples.

Fig. S5 shows the photocatalytic activities of the as-prepared samples under simulated light irradiation. Almost no H_2 is generated on MoP/CC. The H_2 evolution amount of TiO_2/CC is slightly larger than that of TiO_2/CC-N_2. Nevertheless, the composite of TiO_2/MoP/CC-*x* (*x* = 0.6, 2.6, 3.0 and 3.6) display significantly enhanced photocatalytic activity compared with TiO_2/CC and MoP/CC.

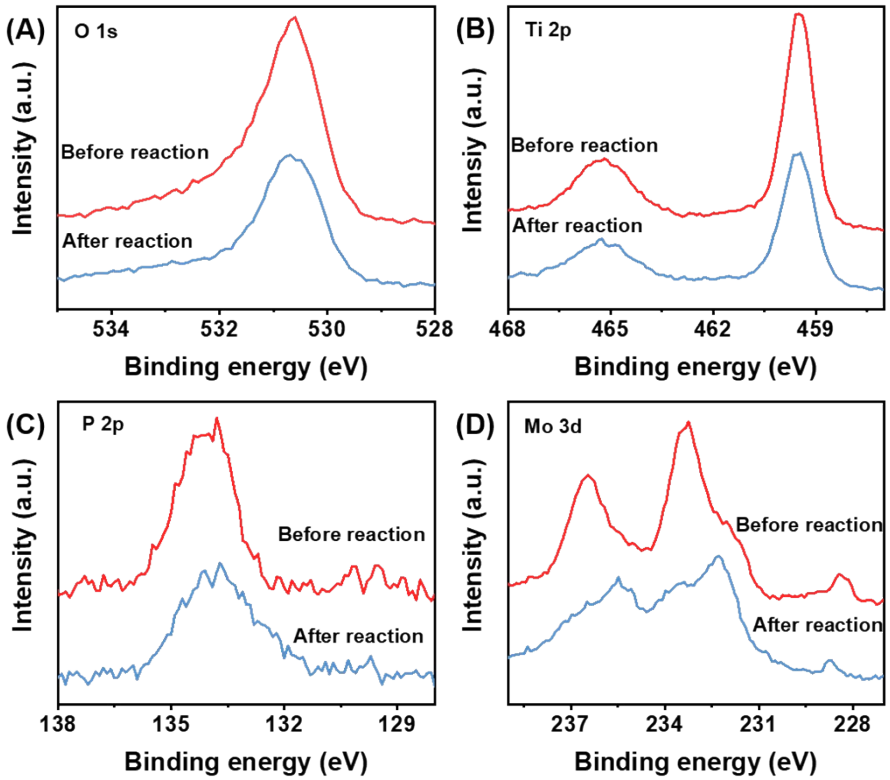

Fig. S6 XPS spectra of (A) O 1s, (B) Ti 2p, (C) P 2p and (D) Mo 3d for TiO_2/MoP/CC sample before and after long-term photocatalytic tests.

In Fig. S6, no obvious change of the high-resolution O 1s, Ti 2p, P 2p and Mo 3d XPS spectra of TiO_2/MoP/CC sample is found before and after long-term photocatalytic tests.

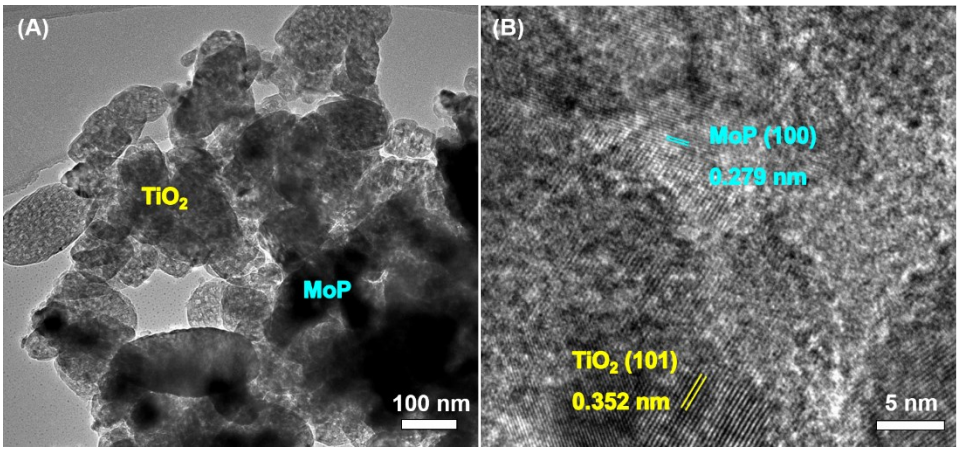

Fig. S7 (A) TEM and (B) HRTEM images of TiO_2/MoP/CC sample after long-term photocatalytic H_2 evolution tests.

It is clear that both TiO_2 and MoP can be seen in TiO_2/MoP/CC sample, elucidating that the continuous recycling tests can not destroy the heterojunction structure of TiO_2/MoP, suggesting its high stability.

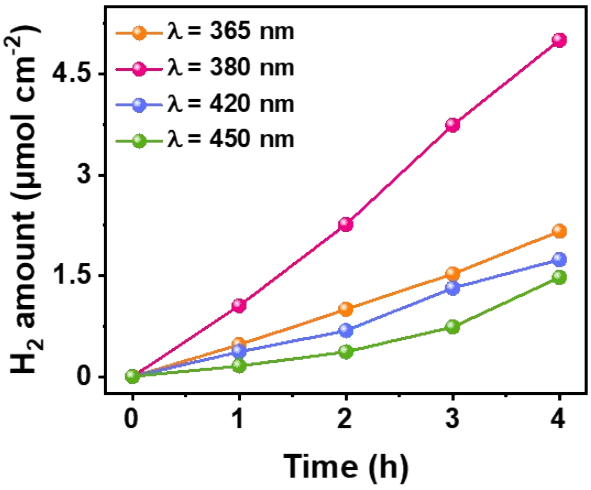

Fig. S8 Time course of H_2 generation of TiO_2/MoP/CC under illumination of 365, 380, 420 and 450 nm in 10 vol% of triethanolamine aqueous solution.

Fig. S8 shows the H_2 generation amount as a function of time over TiO_2/MoP/CC under illumination of different incident wavelengths. The apparent quantum yield (AQY) can be calculated according to the following Eq. S1:

$$AQY(\%) = \frac{2 \times Number\ of\ evolved\ H_2\ molecules}{Number\ of\ incident\ photons} \times 100\% = \frac{2N1}{N2} \times 100\%\ (S1)$$

where N1 and N2 represent the number of evolved H_2 molecules and incident photons, respectively.

Here, taken the incident wavelength of 365 nm as an example, $N1 = H_2\ evolution\ amount \times Avogadro's\ Constant$, where the value of Avogadro's constant is 6.022×10^{23} mol^{-1}. $N2 = \frac{E\lambda}{hc}$, where E is the power of Xe lamp (2.818 W m^{-2}), λ is the incident wavelength (365×10^{-9} m), h is the Planck's constant (6.63×10^{-34} J·s), c is the speed of light (3.0×10^8 m s^{-1}), and the irradiation area is 38.48 cm^2. In addition, the reation time is 1.44×10^4 s. Then, the value of N1 and N2 are calculated to be 1.30×10^{18} and 2.87×10^{20}, respectively. As a result, the apparent quantum yield of TiO_2/MoP/CC is 0.906% at 365 nm irradiation.

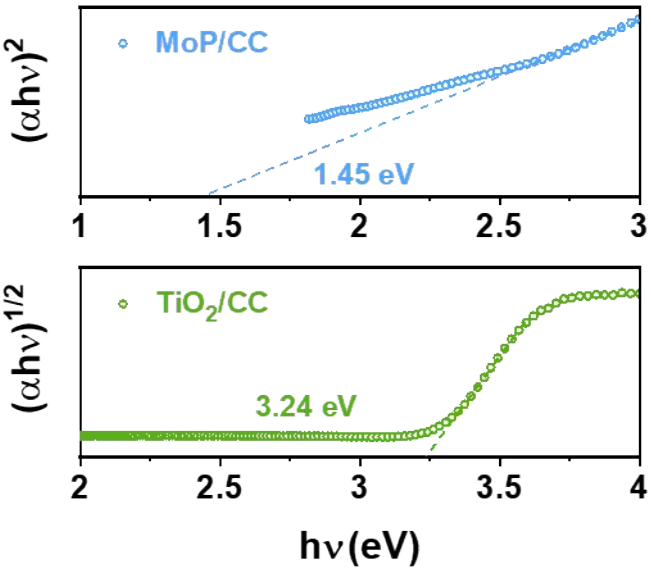

Fig. S9. Tauc plots of TiO_2/CC and MoP/CC samples derived from their UV-vis DRS.

Fig. S9 shows the Tauc plots $(\alpha hv)^n$ (n = 2 and 1/2 for direct and indirect semiconductors, respectively) of MoP/CC and TiO_2/CC as a function of photonic energy (hv).

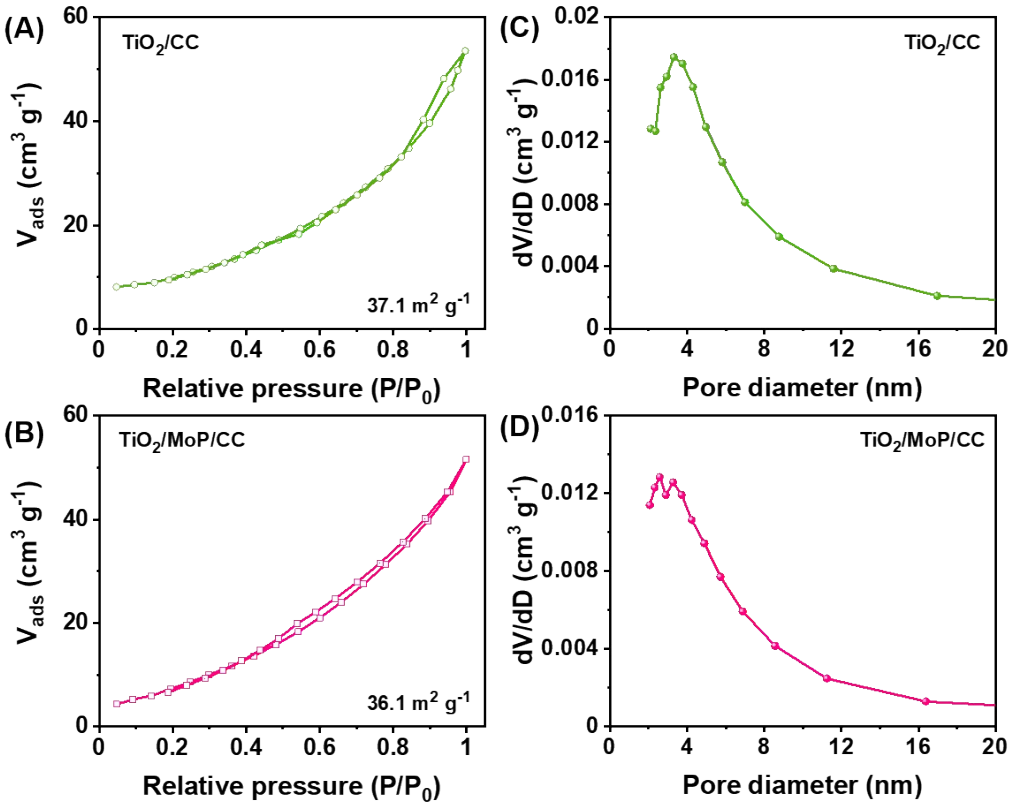

Fig. S10 (A,B) N_2 adsorption-desorption isothermal curves and (C,D) BJH pore diameter distribution of TiO_2 and TiO_2/MoP/CC, respectively.

N_2 adsorption-desorption isotherms were carried out to explore the Brunauer-Emmett-Teller (BET) surface area of the as-prepared photocatalysts. As shown in Fig. S10, both TiO_2/CC and TiO_2/MoP/CC display type Ⅳ isotherms with type H3 hysteresis loop, suggesting the presence of mesopore structure.[1,2]

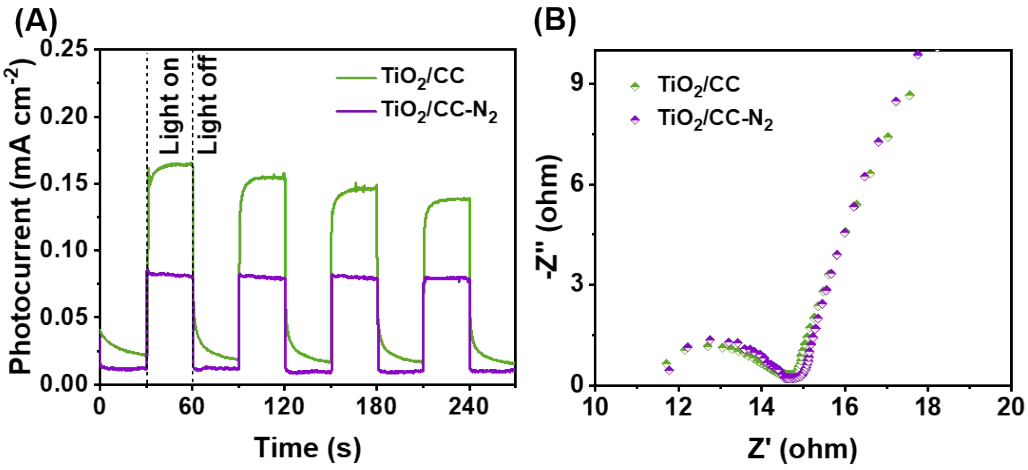

Fig. S11 (A) Current-time responses and (B) electrochemical impedance spectroscopy Nyquist plots of TiO_2/CC and TiO_2/CC-N_2.

It can be seen in Fig. S11 that TiO_2/CC exhibits larger photocurrent and smaller charge transfer resistance than that of TiO_2/CC-N_2.

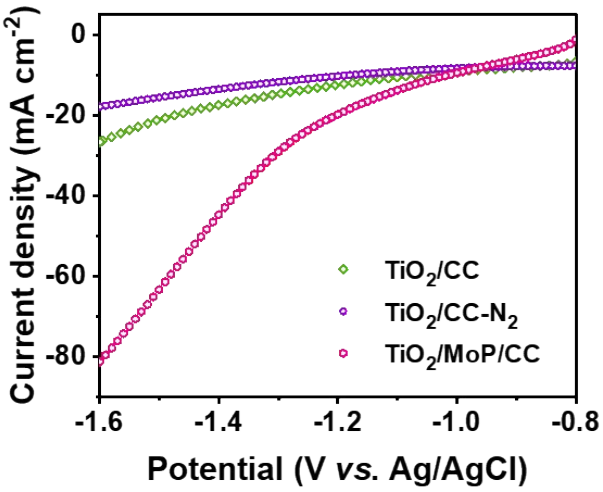

Fig. S12 Linear sweep voltammetric curves of TiO_2/CC, TiO_2/CC-N_2 and TiO_2/MoP/CC obtained in 1 M KOH electrolyte in dark condition.

Fig. S12 shows the linear sweep voltammetric curves of TiO_2/CC, TiO_2/CC-N_2 and TiO_2/MoP/CC in 1 M KOH solution. It can be clearly seen that TiO_2/MoP/CC shows the largest cathodic current density and smallest overpotential among the three samples.

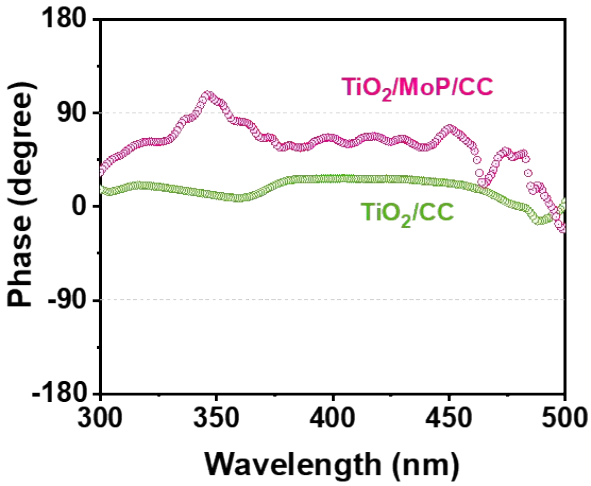

Fig. S13 The phase spectra of TiO_2/CC and TiO_2/MoP/CC samples obtained from the SPV spectra.

Generally, the phase values in quadrants I and IV (0 to ±90°) indicate the holes transfer to the surface, whereas the electrons move to the surface when the phase values locate in quadrant II and III (±90 to ±180°). As shown in Fig. S13, both phase values of TiO_2/CC and TiO_2/MoP/CC in quadrants I and IV region are observed.

3. Supplementary Tables

Table S1. The loading amount of MoP and TiO_2 in TiO_2/MoP/CC-*x* (*x* = 0.6, 2.6, 3.0 and 3.6).

Sample	m_{MoP} (mg)	m_{TiO_2} (mg)	m_{MoP}/m_{TiO_2} (wt%)
TiO_2/MoP/CC-0.6	0.6	12.8	4.7
TiO_2/MoP/CC-2.6	2.6	12.8	20.3
TiO_2/MoP/CC-3.0	3.0	12.8	23.4
TiO_2/MoP/CC-3.6	3.6	12.8	28.1

Table S2. The specific resistance values of EIS plots of TiO_2/CC and TiO_2/MoP/CC in dark condition.

Sample	R_s (Ω)	R_{ct} (Ω)
TiO_2/CC	12.0	2.4
TiO_2/MoP/CC	11.3	1.5

4. Supplemental references

S1. L.-L. Zhang, H.-W. Zhang, B. Wang, X.-Y. Huang, Y. Ye, R. Lei, W.-H. Feng and P. Liu, A facile method for regulating the charge transfer route of WO_3/CdS in high-efficiency hydrogen production, *Appl. Catal. B Environ.*, 2019, **244**, 529-535.

S2. C. Xue, P. Zhang, G.-S. Shao and G.-D. Yang, Effective promotion of spacial charge separation in direct Z-scheme WO_3/CdS/WS_2 tandem heterojunction with enhanced visible-light-driven photocatalytic H_2 evolution, *Chem. Eng. J.*, 2020, **398**, 125602.